Atmospheric Gravity Waves in Aeolus Wind Lidar Observations

T. P. Banyard[1], C. J. Wright[1], N. P. Hindley[1], G. Halloran[2], I. Krisch[3], B. Kaifler[3], L. Hoffmann[4]

[1]Centre for Space, Atmospheric and Oceanic Science, University of Bath, Bath, United Kingdom
[2]Met Office, Exeter, United Kingdom
[3]DLR, Institut für Physik der Atmosphäre, Oberpfaffenhofen, Germany
[4]Jülich Supercomputing Centre, Forschungszentrum Jlich, Jlich, Germany

Key Points:

- First satellite observations of atmospheric gravity waves using ADM-Aeolus
- A case study is presented of an orographic gravity wave over the Southern Andes, with coherent phase structure down to the surface
- Results reproduce well in satellite observations and reanalysis data

Corresponding author: T. P. Banyard, tpb38@bath.ac.uk

Abstract

Aeolus is the first Doppler wind lidar in space. It provides unique high-resolution measurements of horizontal wind in the sparsely-observed upper-troposphere/lower-stratosphere (UTLS), with global coverage. In this study, Aeolus' ability to resolve atmospheric gravity waves (GWs) is demonstrated. The accurate representation of these small-scale waves is vital to properly simulate dynamics in global weather and climate models. In a case study over the Andes, Aeolus GW measurements show coherent phase structure from the surface to the lower stratosphere, with wind perturbations >10 ms^{-1}, a vertical wavelength ∼8 km and an along-track horizontal wavelength ∼900 km. Good agreement is found between Aeolus and colocated satellite, ground-based lidar and reanalysis data sets for this example. Our results show that data from satellites of this type can provide unique information on GW sources and propagation in the UTLS, filling a key knowledge gap that underlies known major deficiencies in weather and climate modelling.

Plain Language Summary

Gravity waves are an important driver of the global atmospheric circulation but are difficult to observe due to their scale size and location. Existing satellite observations reveal these waves in temperature perturbations, but tend to be limited in either vertical or horizontal resolution. Since they are arguably best described in a wind-based mathematical framework and due to their influential behaviour in the upper-troposphere lower-stratosphere region, an observing platform that satisfies both of these requirements could prove very significant. This study explores the capability of the first Doppler wind lidar in space, Aeolus, to measure gravity waves and provide unique information about their sources and propagation through the atmosphere. Significantly, Aeolus measures wind speed directly and is well suited to observe the upper-troposphere lower-stratosphere region. Here, a case study is presented showing observations of a strong gravity wave produced by the enhanced orography of the Southern Andes, which are the most prominent hotspot of gravity wave activity globally. Results are validated against two other observational instruments and atmospheric reanalysis, and give confidence in Aeolus' ability to measure these phenomena.

1 Introduction

Atmospheric gravity waves (GWs) are small-scale propagating disturbances that arise due to the vertical forcing of air parcels by a disturbance in the flow. They are generated by a variety of meteorological processes, including flow over orography, atmospheric deep convection, and jet stream, cyclonic and frontal instabilities. GWs play a wide range of key roles in the atmospheric system, particularly in the transfer of energy and momentum (e.g. Fritts & Alexander, 2003). They are responsible for driving the large-scale circulation in the middle atmosphere, primarily through accelerations to the mean-flow by the convergence of GW momentum flux (Fritts, 1984). They also modulate phenomena such as the Quasi-Biennial Oscillation (Dunkerton, 1997; Ern et al., 2014), affect stratosphere-mesosphere coupling during Sudden Stratospheric Warmings (Siskind et al., 2007; Wright et al., 2010), and can produce turbulence when they dissipate that is dangerous to aircraft (Lilly, 1978; Bramberger et al., 2018).

Both climate and numerical weather prediction (NWP) models rely on accurately representing the propagation of GWs from sources near the surface to the upper-troposphere/lower-stratosphere (UTLS) region. This accuracy is needed to correctly simulate important features of the atmosphere such as the strength of the northern and southern hemispheric jet streams (Holton, 1983; McFarlane, 1987; M. Alexander et al., 2010; Sato et al., 2012; Ehard et al., 2017). As such, limited understanding of the drag forces GWs exert on the

mean winds has historically proven to be a significant barrier to advances in NWP, and improvements in GW simulation have often led to model-wide improvements across a range of processes and scales (Palmer et al., 1986; Eichinger et al., 2020). As model resolutions continue to improve, particularly in the vertical dimension, capturing GW processes is becoming an increasingly important problem, and this trend is likely to continue in the near future (Jones et al., 1997; Kim et al., 2003; Watanabe et al., 2015).

Most GWs are currently parameterised in general circulation models (GCMs) (M. Alexander & Barnet, 2007; Geller et al., 2013). However, in practice these parameterisations are not well constrained observationally, due to both the relatively small spatial scales of most GWs and because the GW field varies dramatically across a large range of spatiotemporal frequencies (M. J. Alexander, 1998; M. Alexander et al., 2010). This has long been identified as an important knowledge gap, and since the first empirical measurements of GWs (Hines, 1960), observations have been made using a wide variety of methods.

In-situ observations such as those from radiosondes, aircraft and meteorological rockets often form an anchor point against which other measurements can be validated (B. Sun et al., 2010; Krisch et al., 2017). Satellite-based observations of GWs are provided by nadir-sounders such as AIRS and AMSU, as well as limb-sounders such as HIRDLS and the COSMIC GPS constellation. These instruments typically measure infra-red radiances, from which wind perturbations must be inferred using a set of GW dispersion relations (Ern et al., 2004; Hindley et al., 2015; Wright, Hindley, & Mitchell, 2016; Wright, Hindley, Moss, & Mitchell, 2016). Finally, there are ground-based radars and lidars, which provide good temporal coverage at a reasonable vertical resolution (N. Kaifler et al., 2020). These however are fixed to one location and cannot provide a global climatology of GW activity by themselves.

Radars and lidars in particular provide direct measurements of the wind perturbations induced by GWs (e.g. Larsen et al., 1982; Vincent & Reid, 1983), which is important because GWs are arguably best-described at a theoretical level in a wind-based mathematical framework. However, the existing inability to systematically measure winds from space means that relatively few GW measurements have been made using wind perturbations directly other than at these radar and lidar sites, and none to date on a global domain. In 2018 however, the first spaceborne wind lidar instrument was launched aboard the European Space Agencys Aeolus mission. This novel ability to systematically measure winds from space offers the potential to significantly advance our understanding of how GWs propagate in the real atmosphere, and in turn to advance weather and climate modelling.

To demonstrate the benefits of using Aeolus and its proposed successors as a platform for systematic GW observations, presented here is a case study using Aeolus data to examine the structure of a large GW observed in winter (July) 2019 over the Andes mountains. The Andes are a fantastic natural laboratory for observing GWs due to the ridge at their southern end which is transverse to the prevailing westerly winds. Globally, the Andes are by far the most prominent hotspot of GW activity, and the strong orographic forcing often present can produce waves of large magnitude which propagate significant distances into the middle and upper atmosphere (Jiang et al., 2002; M. Alexander & Teitelbaum, 2011; Hoffmann et al., 2013). Additionally, Aeolus' high inclination orbit is oriented approximately parallel to the southern Andean ridge line, measuring a horizontal line-of-sight (HLOS) wind that is close to zonal and approximately transverse to the mountains at this latitude. Detection conditions here are therefore well-suited for a study of this type, which will be generalised to more complicated cases at the global scale in future work.

Section 2 describes the data sources and methodology for this study, with an outline of both Aeolus and the other observing systems that are used to validate these mea-

surements. Section 3 shows the first example of GWs measured in Aeolus data, and uses other observations and ERA5 reanalysis to validate these results. Section 4 discusses the limitations of the methods used and summarises the key points from this study.

2 Data and Methods

The purpose of this case study is to determine whether Aeolus is a suitable platform for observing GWs, and to give a first suggestion of the possibilities it presents for wider GW studies. First, a large GW event on the 26th July 2019 is established as a good candidate using carefully selected along-track vertical profiles from Aeolus. The data is detrended using a band-pass filter to extract wind perturbations, and the coinciding meteorological and geographical context is assessed to determine if the observed GW structure is plausible.

Validation of this GW event in the Aeolus observations is then carried out using data from the CORAL lidar in Tierra del Fuego, the AIRS instrument onboard the Aqua satellite, and output from the ERA5 reanalysis. For the comparison between each, an Aeolus profile which provides a good demonstration of the broader GW signature is empirically selected, and then co-location profiles from CORAL, AIRS and ERA5 are found nearby in time and space. Differences between the datasets mean slightly different procedures are required to extract GW perturbations for each, as described below.

2.1 Aeolus

Aeolus is the first satellite with a space-borne wind lidar instrument onboard (ESA, 1989, 2008; Chanin et al., 1989; Stoffelen et al., 2005; Reitebuch, 2012). This instrument, known as the Atmospheric Laser Doppler Instrument (ALADIN), probes the lowermost 30 km of the atmosphere and provides high vertical resolution profiles of wind, aerosol and cloud along its orbital path. The satellite has a sun-sychronous orbit with 15.6 orbits per day and a repeat cycle of 7 days. The orbit's inclination is 96.97° and its mean altitude is 320 km, with an ascending-node local equator-crossing time of 18:00. Both the laser and telescope are directed at 35° off-nadir, perpendicular to the direction of travel.

A single wind component v_{LOS} is measured along this line-of-sight (LOS), which is converted into the HLOS wind speed v_{HLOS} by assuming the vertical wind speed w is small. Equations (1) and (2) show how these parameters relate to the three cartesian wind components u, v and w; where θ is the elevation of the target-to-satellite pointing vector (55°) and Ψ is the bearing of the satellite track.

$$v_{\mathrm{LOS}} = v_{\mathrm{HLOS}} \cos(\theta) + w \sin(\theta) \tag{1}$$

$$v_{\mathrm{HLOS}} = -u \sin(\Psi) - v \cos(\Psi) \tag{2}$$

ALADIN measures backscattering from atmospheric molecules (Rayleigh scattering), and aerosol and hydrometeors (Mie scattering) in the path of light from its laser, which is operated at a wavelength of 355 nm. The backscattered light is received using a 55 kg telescope which is 1.5 m in diameter, and the Doppler shift of this signal relative to the laser pulse frequency is recorded. These data are processed to produce a measurement of the HLOS wind speed for both Mie and Rayleigh scattering, throughout the depth of the atmospheric profile (Rennie et al., 2020). The vertical levels are split into range bins which are between 250-2000m in depth and can be chosen and altered from the ground, with the instrument arranging data into these bins according to the time difference between the laser pulse being transmitted and the return signal being received.

Aeolus data used in this study are aggregated into profiles according to grouping identifiers within each file (De Kloe et al., 2020). We use the L2B product; for this prod-

uct, each observation is categorised as occurring in either clear or cloudy conditions, and an associated HLOS error estimate is also provided for quality control. Only Rayleigh clear observations are used in this study to maximise data coverage in combination with data quality. An 8 ms^{-1} cut off is used as a filter on the random error for each data point. The data used here has been reprocessed using baseline B10 of ESA's L2B processor. A number of campaigns have validated the HLOS winds from Aeolus, with the latest estimates for this reprocessed data showing a systematic bias of <1 ms^{-1} for the Rayleigh wind product (Abdalla et al., 2020). Since this study is primarily concerned with wind perturbations, any systematic biases in the data are considered to have a negligible impact on the results.

To plot along-track profiles, the data are linearly interpolated onto a 500m vertical grid. Wind perturbations are then calculated by running an along-track Savitzky-Golay bandpass filter through the data points, with lower and upper bounds of 7 and 25 profiles respectively. GWs with along-track horizontal wavelengths of ∼6002000 km are detectable using this method. This detrending method is chosen because it best highlights the orientation of the GW for this particular case study. Unlike at higher altitudes, there is no clear scale separation between GWs and other atmospheric features; such as jet streaks, synoptic-scale Rossby waves and various mesoscale phenomena (Perlwitz & Graf, 2001; C. Sun et al., 2014). In this example, the low cutoff point should remove smaller-scale perturbations which might not be related to GW activity, however caution ought to be applied if using this detrending method in the general case.

2.2 CORAL lidar

The Compact Rayleigh Autonomous Lidar (CORAL) instrument is an autonomous ground-based lidar system designed to provide temperature and density profiles of the middle atmosphere (B. Kaifler & Kaifler, 2020). Situated at Tierra del Fuego on the southern tip of South America (54°S, 68°W), it is positioned at a prime location for measuring strong orographic GW activity (N. Kaifler et al., 2020). The altitude range covered by CORAL measurements extends from 15 – 90 km, and measurements have a 900 m vertical resolution oversampled onto a 90 m grid, with a temporal resolution of 20 min. CORAL measures backscattered photons detected in three Rayleigh channels (532 nm) and one Raman channel (608 nm), in clear-sky conditions only. In this study, the Raman channel is used for altitudes below 31 km.

As discussed by Ehard et al. (2015), estimating temperature perturbations using a lidar such as CORAL can be challenging, especially where there are sudden changes in the vertical temperature gradient, such as at the stratopause. Using temporal filtering would alleviate this issue, however due to the short observational periods on this particular day, such a method is not possible for this case study. Instead, to obtain temperature perturbations a vertical Savitzky-Golay high-pass filter is run with a cut-off wavelength of 20 km. This is in line with previous studies (e.g. B. Kaifler et al., 2015; N. Kaifler et al., 2020) and should be sufficient to observe the important characteristics of this GW.

2.3 AIRS

The Atmospheric Infrared Sounder (AIRS) is a 2378-channel infrared nadir sounder onboard NASA's Aqua satellite (Aumann et al., 2003; Chahine et al., 2006). Part of the A-Train satellite constellation, Aqua is in a sun-synchronous orbit with 14.55 orbits per day, a repeat cycle of 16 days, an orbital inclination of 98.20° and an ascending-node local equator-crossing time of 13:30. The AIRS instrument scans across track in a ±49.5° wide swath, measuring radiances. The horizontal resolution varies from ∼13.5 km × 13.5 km at nadir to 41 km × 21.4 km at the track edge, and measurement data are stored in "granules", each corresponding to 6 minutes of data (Wright et al., 2017).

In order to provide enough context for the Aeolus overpass, one AIRS granule before and one after the Aeolus overpass are chosen, each with good spatial coverage of the Southern Andes. The retrieval outlined by Hoffmann and Alexander (2009) has been used to estimate air temperature on a 3 km vertical grid from 18–55 km altitude, and results are shown at the 30 km altitude level to avoid vertical edge-truncation effects and as a representative snapshot. Temperature perturbations have been calculated by running a cross-track 4th-order polynomial fit through the data as demonstrated in M. Alexander and Barnet (2007). GWs with cross-track horizontal wavelengths of ∼50–1000 km are detectable using this method (e.g. Hoffmann et al., 2014; Ern et al., 2016).

2.4 ERA5

ERA5 is a reanalysis dataset provided by the ECMWF which combines an Earth-system model with assimilated observations to provide a historical archive of the state of the atmosphere (Hersbach et al., 2020). The dataset has a spatial resolution of $0.25\,^\circ \times 0.25\,^\circ$ (∼31 km), 137 vertical levels from the surface up to 0.1 hPa, and a temporal resolution of one hour. Since Aeolus observations are not assimilated into ERA5, the two datasets are entirely independent from each other. As the Aeolus overpass studied here occurs at almost exactly 10:00, this is also the time chosen for the ERA5 vertical profile. In order to directly compare data from the Aeolus overpass with ERA5, the latter is interpolated bi-linearly onto each Aeolus measurement point in space. This is done by projecting the ERA5 u and v wind components onto the Aeolus comparable HLOS, as shown in equation (2). The data are then further interpolated onto the same 500 m vertical grid as done previously, so that the same horizontal Savitzky-Golay filtering approach can be used. For the multi-dataset validation of the GW, the single nearest ERA5 profile to the chosen Aeolus profile is selected rather than interpolating to the measurement location, in order to avoid any aliasing caused by averaging between data points.

Topographical context is provided using $0.25\,^\circ \times 0.25\,^\circ$ resolution elevation data from the TBASE archive provided by NCAR, and the elevation for each profile is calculated using a bi-linear interpolation of this dataset. Mean Sea-Level Pressure (MSLP) and cloud fraction layers for the meteorological context are also provided from hourly ERA5 data at a $0.25\,^\circ \times 0.25\,^\circ$ resolution.

3 Results

Figure 1 demonstrates clearly for the first time that GWs can be observed using space-borne wind lidar instruments. The figure shows winds measured during an Aeolus pass over the Andes mountain range on the 26th July 2019. The meteorological context is a deep depression to the west of the Drake Passage, which drives a strong westerly wind over the raised topography of the Southern Andes. This pattern causes significant surface wind stresses, which typically translate to strong upward-propagating orographic GWs; such a source mechanism is consistent with the characteristics of the wave observed here. Aeolus is on the descending node of its orbit at this time, and travels down the length of South America before intersecting the mountain range and heading out over the southern Pacific Ocean. The cloud fraction overlay from ERA5 at the same time shows clear skies along much of the satellite ground-track, providing confidence that it is appropriate to use the Rayleigh-clear HLOS wind product.

The wave itself can be seen clearly in the HLOS wind field between 10:00 and 10:02 in Figure 1b as absolute measured values and in Figure 1c as perturbations to the background wind field. It coincides geographically with a region of raised topography and appears to be propagating upwards into the stratosphere with a vertical wavelength of around 8 km and an amplitude of around 10 m/s. Also of note is the polar night jet, which can be seen in the lower stratosphere south of 50°S. The Savitzky-Golay filtering em-

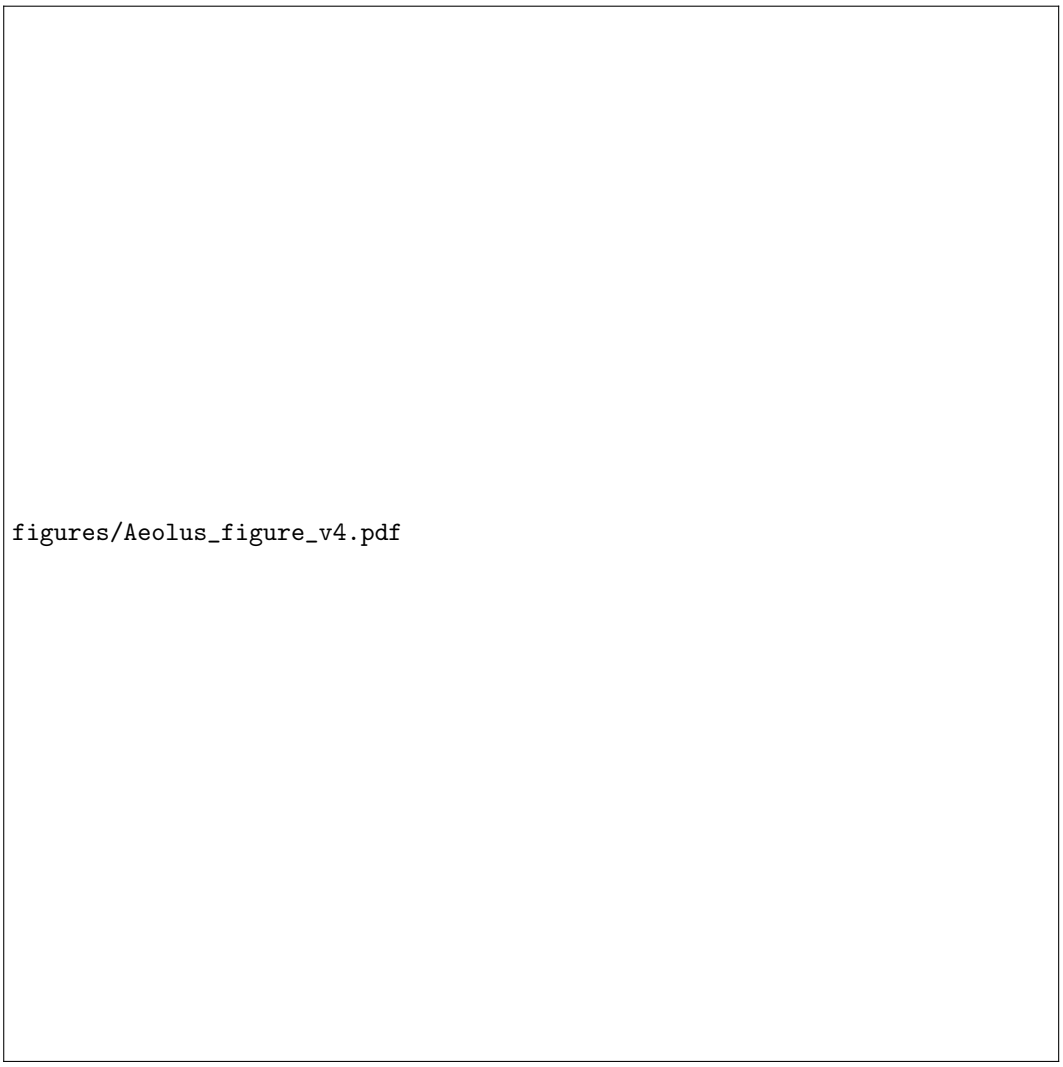

Figure 1. Aeolus overpass of 2019-07-26 with a) a map showing its geographical context, overlayed with ERA5 data on a single-level for cloud fraction and mean sea-level pressure, and terrain data from the TerrainBase Global Terrain Model; b) raw winds in an along-track time-series of the L2B HLOS Rayleigh wind speed product, with colour range set by the mean and two standard deviations of the domain; c) wind perturbations calculated using a 5 - 25 data point Savitzky-Golay band pass filter. Cloudy or missing data points are obscured with a grey mask. The profile used for the validation of the GW in Aeolus is marked with a black arrow, and corresponds to 2019-07-26 10:00:34.

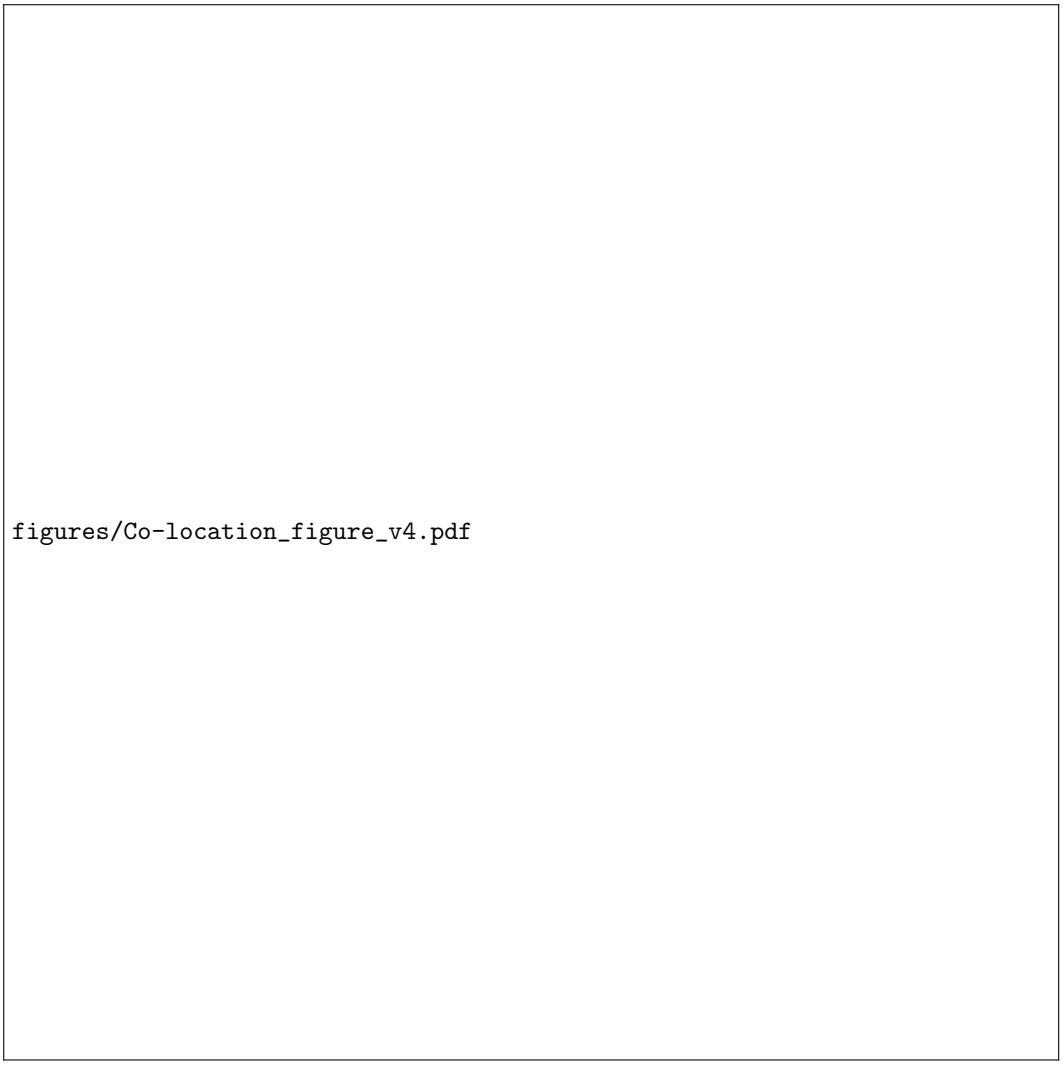

Figure 2. a) Timeseries of kinetic temperature perturbations from the CORAL lidar at Tierra del Fuego for 2019-07-26 at 15 minute resolution. b,c) Data granules 55 and 190 from the AIRS instrument for 05:32 and 19:02 respectively and at an altitude of 30 km. d) 3 time snapshots comparing data from Aeolus with CORAL and AIRS observations and ERA5 reanalysis. AIRS has been multiplied by 0.5 for ease of comparison.

phasises the GW in the wind perturbations in Figure 1c, showing diagonally oriented wave fronts which are most pronounced during the same time-frame.

Validation of the GW seen in the Aeolus data has been carried out using the CORAL lidar, AIRS, and ERA5 reanalysis, and is shown in Figure 2. Distinct quasi-stationary wave-fronts can be seen in the CORAL lidar timeseries (Figure 2a), with a vertical wavelength of around 10 km and an amplitude of around 15 K peaking near the stratopause. AIRS overpasses from before and after the Aeolus pass also show very pronounced GW structures emanating eastwards from the Southern Andes (Figure 2b-c).

Figure 2d shows a comparison between a selected profile from the 10am Aeolus overpass and co-located profiles from each observing system, further contextualised with the nearest ERA5 profile in both temperature and projected HLOS wind. All measurements

are taken from geographically close to the Aeolus profile location, with the exception of the CORAL lidar, which is some 600 km to its south-east. Since the plot shows a combination of temperature and wind measurements, it is important to note that according to theory there is an expected phase difference of 90° between these two fundamental variables.

Between 5-6am strong temperature perturbations can be seen in both CORAL and AIRS, increasing in amplitude with height. The vertical positions of the AIRS temperature peaks match well with CORAL at 25 and 37 km, but appear to be in anti-phase around 50 km. The likely reason for this is the poor vertical resolution of AIRS which aliases the wave; this issue is explored further in Section 4. ERA5 at the same time also shows perturbations in both temperature and wind, particularly below 20 km in the wind profile. Once again there are phase differences with AIRS which are likely a result of aliasing, whereas the differences with CORAL are more likely to be a consequence of the 600 km distance between the two profiles.

At 10am there is very good agreement between the Aeolus and ERA5 wind profiles, particularly in wave amplitude, although with a slight vertical phase offset which increases gradually with height. The large temperature perturbations in the CORAL profile confirm the expectation of strong GW activity coinciding with the Aeolus overpass. The relative change in amplitude at each height between 5-6am and 10am is consistent with ERA5. The reanalysis however does not quite capture the amplitude that CORAL does, which could be a consequence of either the wave dissipating too quickly in the reanalysis model, or the stratopause interfering with the filtering process for CORAL.

At 7pm, only the AIRS observations are available for comparison, and this particular profile shows the wave structure from 5-6am largely persisting through the day until the 7pm overpass. It is difficult to compare with ERA5 due to the significant deficiencies in both datasets, especially at higher altitudes, however the most notable observation is the presence of a persistent large amplitude GW in each. Throughout the measurement period, the amplitude of the wave in AIRS is significant larger than in the other datasets. The reasons for this are unclear but may involve either inaccurate model physics or our choice of detrending approach.

Figure 3 shows ERA5 data projected onto the HLOS wind points observed by Aeolus. The middle and right panels show striking morphological agreement with Figures 1b and 1c. As in the observations, we see a strong orographic GW propagating upwards into the stratosphere above the sharp topography of the Andean ridge. The vertical wavelength is of a similar magnitude to that seen in the Aeolus observations, although importantly the amplitude is not as high as in the Aeolus data, suggesting the model may have a tendency to underestimate the amplitude of such waves as well as exhibiting the phase differences described above.

4 Discussion and Conclusions

The primary limitation for measuring GWs using Aeolus is the complex dynamics of the troposphere and the challenges this presents when detrending the observed data to identify wave perturbations. Unlike in the stratosphere and above, where there is a clear spectral difference between GW perturbations and planetary wave activity or other non-GW related phenomena, in the troposphere a host of meteorological processes can interfere with the analysis. While we have addressed this problem in this case study by empirically selecting a filter length which highlights well the wave of interest, solving this problem in the general case is a larger technical challenge, and will require significant research before our results can be generalised to the global scale (e.g Rapp et al., 2018).

A further limitation is that Aeolus only measures in one wind direction and only provides data along its flight track. Thus, no information about the orientation or real

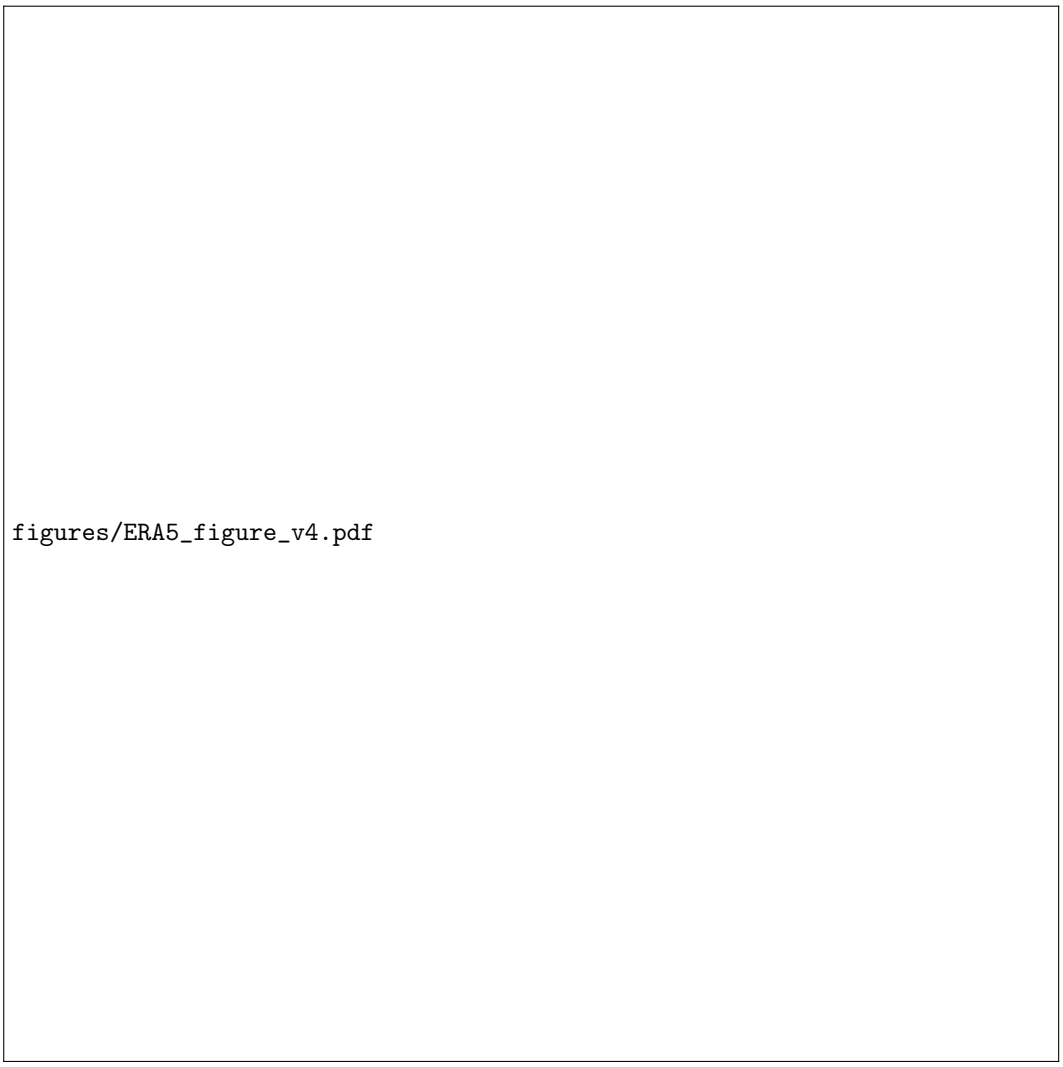

Figure 3. ERA5 validation of the Aeolus overpass of 2019-07-26 with a) a map showing its geographical context, overlayed with ERA5 data on a single-level for cloud fraction and mean sea-level pressure, and terrain data from the TerrainBase Global Terrain Model; b) ERA5 HLOS projected winds to match with the Aeolus along-track profile, with colour range set by the mean and two standard deviations of the domain; c) wind perturbations calculated using a 5 - 25 data point Savitzky-Golay band pass filter. Cloudy or missing data points are obscured with a grey mask. The profile used for the validation of the GW in Aeolus is marked with a black arrow, and corresponds to 2019-07-26 10:00:34.

horizontal wavelength of the measured GWs can be inferred. Instead, only the projection of the horizontal wavelength along the satellite track can be determined, which usually gives an overestimation of the real horizontal wavelength. In the case of orographic GWs over the Andes, this poses a strong restriction on the information Aeolus can provide about their horizontal structure; especially when the satellite bearing is near-parallel to the mountain range as is the case in this study.

Additionally, the HLOS wind calculation of the Aeolus L2B processor assumes a vertical wind of 0 ms^{-1}. This is unproblematic under normal conditions, however where there is strong GW activity this assumption is less justified due to the strong vertical motions that can be present. Since for all structures observed by Aeolus the horizontal domain dominates, regions where the real vertical wind w is large tend to be too small to be resolved. For the GW presented in this paper, the error in the HLOS wind is determined to be below 2%; a figure that can be calculated using the gravity wave polarisation relations (Fritts & Alexander, 2003). Further to this, the orientation of the HLOS winds is not near-zonal close to the pole, leading to a strong bias of the measured waves with respect to latitude. This again may add additional technical difficulties for any global studies of GW activity using data from Aeolus.

Finally, there remain the general problems of filtering for and spectrally analysing GWs in observational data, a problem extensively discussed by e.g. Preusse et al. (2008); Wright, Hindley, Moss, and Mitchell (2016); Strube et al. (2020); Krisch et al. (2020), among others. The data here have been interpolated onto a regular grid in order to carry out the Savitzky-Golay filtering, a process which itself will tend to smooth the peaks of each wave and reduce their amplitude. Furthermore, the transmission of the filter used is inherently imperfect within the wavelength window analysed; this is a general problem for spectral analysis, but one which adds to the uncertainties in such work. Here, as in Hindley et al. (2015), the Savitzky-Golay filter is selected as a trade-off between a desirably sharp transition at each end and Gibbs ringing at the discontinuity, but it will be important to assess how well alternative filters perform in more general future work.

Nonetheless, the strong morphological and quantitative agreement in wave properties between the HLOS wind profiles from Aeolus and the temperature based profiles from CORAL and AIRS leads to a high level of confidence in Aeolus' ability to observe GWs. A clear phase structure is visible from near the surface up to the stratosphere, with the CORAL lidar supplementing this higher up and AIRS providing information about its geographical orientation. Good qualitative agreement is found between these wind and temperature measurements, suggesting that good phase relationship is observed, even if there is sometimes a phase offset from one location to the next. Our results demonstrate the benefit of these spaceborne wind lidar measurements for GW studies, which can be used to better constrain GW parameterisations in models and improve our understanding of small-scale GW processes.

Data Availability Statement

Aeolus data were provided by the European Space Agency, and can be accessed via https://aeolus-ds.eo.esa.int/oads/access/. The AIRS data were provided by NASA; L1 radiance data can be acquired via https://disc.gsfc.nasa.gov/, and were retrieved to L2 temperatures using the method described by Hoffmann and Alexander (2009). ERA5 data can be accessed from the Copernicus Climate Data Store, https://cds.climate.copernicus.eu/. CORAL Lidar data are not routinely archived publically, but the data used for this study have been archived at https://halo-db.pa.op.dlr.de/dataset/7620.

Acknowledgments

T. P. Banyard is funded by Royal Society grant RGF/EA/180217 and EPSRC. C. J. Wright is funded by Royal Society grant UF160545 and NERC grant NE/S00985X/1. C. J. Wright and N. P. Hindley are funded by NERC grant NE/R001391/1. TPB carried out the research, wrote all computer code and visualisation software, and wrote the majority of the initial draft of the paper. CJW and NPH contributed directly to the initial draft, and also to primary data interpretation and investigation strategies. IK and GH provided significant assistance with data-detrending strategies and understanding the capabilities and limitations of Aeolus data. LH and BK provided and supported the interpretation of non-Aeolus data from AIRS and CORAL, including understanding the capabilities and limitation of these datasets. All authors contributed to finalising the manuscript for submission.

References

Abdalla, S., Aprile, S., Mellano, L., De Laurentis, M., Fischer, P., Von Bismarck, J., ... Isaksen, L. (2020). Aeolus: First FM-B science data reprocessing campaign. *Aeolus CAL/VAL and Science Workshop 2020*.

Alexander, M., & Barnet, C. (2007). Using satellite observations to constrain parameterizations of gravity wave effects for global models. *Journal of the atmospheric sciences*, *64*(5), 1652-1665. doi: 10.1175/JAS3897.1

Alexander, M., Geller, M., McLandress, C., Polavarapu, S., Preusse, P., Sassi, F., ... Kawatani, Y. (2010). Recent developments in gravitywave effects in climate models and the global distribution of gravitywave momentum flux from observations and models. *Quarterly Journal of the Royal Meteorological Society*, *136*(650), 1103-1124. doi: 10.1002/qj.637

Alexander, M., & Teitelbaum, H. (2011). Threedimensional properties of Andes mountain waves observed by satellite: A case study. *Journal of Geophysical Research: Atmospheres*, *116*(D23). doi: 10.1029/2011JD016151

Alexander, M. J. (1998). Interpretations of observed climatological patterns in stratospheric gravity wave variance. *Journal of Geophysical Research: Atmospheres*, *103*(D8), 8627-8640. doi: 10.1029/97JD03325

Aumann, H., Chahine, M., Gautier, C., Goldberg, M., Kalnay, E., McMillin, L., ... Strow, L. (2003). AIRS/AMSU/HSB on the Aqua mission: Design, science objectives, data products, and processing systems. *IEEE Transactions on Geoscience and Remote Sensing*, *41*(2), 253-264. doi: 10.1109/TGRS.2002.808356

Bramberger, M., Drnbrack, A., Wilms, H., Gemsa, S., Raynor, K., & Sharman, R. (2018). Vertically propagating mountain wavesa hazard for high-flying aircraft? *Journal of Applied Meteorology and Climatology*, *57*(9), 1957-1975. doi: 10.1175/JAMC-D-17-0340.1

Chahine, M., Pagano, T., Aumann, H., Atlas, R., Barnet, C., Blaisdell, J., ... Gautier, C. (2006). AIRS: Improving weather forecasting and providing new data on greenhouse gases. *Bulletin of the American Meteorological Society*, *87*(7). doi: 10.1175/BAMS-87-7-911

Chanin, M., Garnier, A., Hauchecorne, A., & Porteneuve, J. (1989). A Doppler lidar for measuring winds in the middle atmosphere. *Geophysical Research Letters*, *16*(11). doi: 10.1029/GL016i011p01273

De Kloe, J., Stoffelen, A., Tan, D., Andersson, E., Rennie, M., Dabas, A., ... Huber, D. (2020). ADM-Aeolus Level-2B/2C Processor Input/Output Data Definitions Interface Control Document. *ESA*, 110p.

Dunkerton, T. (1997). The role of gravity waves in the quasibiennial oscillation. *Journal of Geophysical Research: Atmospheres*, *102*(D22), 26053-26076. doi: 10.1029/96JD02999

Ehard, B., Kaifler, B., Drnbrack, A., Preusse, P., Eckermann, S., Bramberger, M.,

... Rapp, M. (2017). Horizontal propagation of largeamplitude mountain waves into the polar night jet. *Journal of Geophysical Research: Atmospheres*, *122*(3), 1423-1436. doi: 10.1002/2016JD025621

Ehard, B., Kaifler, B., Kaifler, N., & Rapp, M. (2015). Evaluation of methods for gravity wave extraction from middle-atmospheric lidar temperature measurements. *Atmospheric Measurement Techniques*, 4645-4655. doi: 10.5194/amt-8-4645-2015

Eichinger, R., Garny, H., cha, P., Danker, J., Dietmller, S., & Oberlnder-Hayn, S. (2020). Effects of missing gravity waves on stratospheric dynamics; part 1: climatology. *Climate Dynamics*, *54*(5), 31653183. doi: 10.1007/s00382-020-05166-w

Ern, M., Hoffmann, L., & Preusse, P. (2016). Directional gravity wave momentum fluxes in the stratosphere derived from highresolution AIRS temperature data. *Geophysical Research Letters*, *44*(1), 475-485. doi: 10.1002/2016GL072007

Ern, M., Ploeger, F., Preusse, P., Gille, J., Gray, L., Kalisch, S., ... Riese, M. (2014). Interaction of gravity waves with the QBO: A satellite perspective. *Journal of Geophysical Research: Atmospheres*, *119*(5), 2329-2355. doi: 10.1002/2013JD020731

Ern, M., Preusse, P., Alexander, M., & Warner, C. (2004). Absolute values of gravity wave momentum flux derived from satellite data. *Journal of Geophysical Research: Atmospheres*, *109*(D20). doi: 10.1029/2004JD004752

ESA. (1989). ALADIN - Atmospheric Laser Doppler Instrument. Working Group Report. *ESA SP-1112*, 45p.

ESA. (2008). Adm-aeolus science report. *ESA SP-1311*, 121p.

Fritts, D. (1984). Gravity wave saturation in the middle atmosphere: A review of theory and observations. *Reviews of Geophysics*, *22*(3), 275-308. doi: 10.1029/RG022i003p00275

Fritts, D., & Alexander, M. (2003). Gravity wave dynamics and effects in the middle atmosphere. *Reviews of Geophysics*, *41*(1). doi: 10.1029/2001RG000106

Geller, M., Alexander, M., Love, P., Bacmeister, J., Ern, M., Hertzog, A., ... Zhou, T. (2013). A comparison between gravity wave momentum fluxes in observations and climate models. *Journal of Climate*, *26*(17), 6383-6405. doi: 10.1175/JCLI-D-12-00545.1

Hersbach, H., Bell, B., Berrisford, P., Hirahara, S., Hornyi, A., MuozSabater, J., ... Simmons, A. (2020). The ERA5 global reanalysis. *Quarterly Journal of the Royal Meteorological Society*, *146*(730), 1999-2049. doi: 10.1002/qj.3803

Hindley, N., Wright, C., Smith, N., & Mitchell, N. (2015). The southern stratospheric gravity wave hot spot: individual waves and their momentum fluxes measured by COSMIC GPS-RO. *Atmospheric Chemistry and Physics*, *15*(14). doi: 10.5194/acp-15-7797-2015

Hines, C. (1960). Internal atmospheric gravity waves at ionospheric heights. *Canadian Journal of Physics*, *38*(11), 1441-1481. doi: 10.1139/p60-150

Hoffmann, L., & Alexander, M. (2009). Retrieval of stratospheric temperatures from atmospheric infrared sounder radiance measurements for gravity wave studies. *Journal of Geophysical Research: Atmospheres*, *114*(D7). doi: 10.1029/2008JD011241

Hoffmann, L., Alexander, M., Clerbaux, C., Grimsdell, A., Meyer, C., Rler, T., & Tournier, B. (2014). Intercomparison of stratospheric gravity wave observations with AIRS and IASI. *Atmospheric Measurement Techniques*, 45174537. doi: 10.5194/amt-7-4517-2014

Hoffmann, L., Xue, X., & Alexander, M. J. (2013). A global view of stratospheric gravity wave hotspots located with Atmospheric Infrared Sounder observations. *Journal of Geophysical Research: Atmospheres*, *118*(2), 416-434. doi: 10.1029/2012jd018658

Holton, J. R. (1983). The influence of gravity wave breaking on the general circula-

tion of the middle atmosphere. *Journal of Atmospheric Sciences*, *40*(10), 2497-2507. doi: 10.1175/1520-0469(1983)040⟨2497:TIOGWB⟩2.0.CO;2

Jiang, J., Wu, D., & Eckermann, S. (2002). Upper Atmosphere Research Satellite (UARS) MLS observation of mountain waves over the Andes. *Journal of Geophysical Research: Atmospheres*, *107*(D20), SOL-15. doi: 10.1029/2002JD002091

Jones, P., Hamilton, K., & Wilson, R. (1997). A very high resolution general circulation model simulation of the global circulation in austral winter. *Journal of Atmospheric Sciences*, *54*(8), 1107-1116. doi: 10.1175/1520-0469(1997)054⟨1107:AVHRGC⟩2.0.CO;2

Kaifler, B., & Kaifler, N. (2020). A Compact Rayleigh Autonomous Lidar (CORAL) for the middle atmosphere. *Atmospheric Measurement Techniques*, 1-24. doi: 10.5194/amt-2020-418

Kaifler, B., Lbken, F., Hffner, J., Morris, R., & Viehl, T. (2015). Lidar observations of gravity wave activity in the middle atmosphere over Davis (69 S, 78 E), Antarctica. *Journal of Geophysical Research: Atmospheres*, *120*(10). doi: 10.1002/2014JD022879

Kaifler, N., Kaifler, B., Drnbrack, A., Rapp, M., Hormaechea, J. L., & de la Torre, A. (2020). Lidar observations of large-amplitude mountain waves in the stratosphere above Tierra del Fuego, Argentina. *Scientific Reports*, 1-10. doi: 10.1038/s41598-020-71443-7

Kim, Y., Eckermann, S., & Chun, H. (2003). An overview of the past, present and future of gravitywave drag parametrization for numerical climate and weather prediction models. *Atmosphere-Ocean*, *41*(1), 65-98. doi: 10.3137/ao.410105

Krisch, I., Ern, M., Hoffmann, L., Preusse, P., Strube, C., Ungermann, J., ... Riese, M. (2020). Superposition of gravity waves with different propagation characteristics observed by airborne and space-borne infrared sounders. *Atmospheric Chemistry and Physics*, *20*(19), 11469-11490. doi: 10.5194/acp-20-11469-2020

Krisch, I., Preusse, P., Ungermann, J., Drnbrack, A., Eckermann, S. D., Ern, M., ... Riese, M. (2017). First tomographic observations of gravity waves by the infrared limb imager GLORIA. *Atmospheric Chemistry and Physics*, *17*(24), 1493714953. doi: 10.5194/acp-17-14937-2017

Larsen, M., Kelley, M., & Gage, K. (1982). Turbulence spectra in the upper troposphere and lower stratosphere at periods between 2 hours and 40 days. *Journal of the Atmospheric Sciences*, *39*(5), 10351041. doi: 10.1175/1520-0469(1982)039⟨1035:TSITUT⟩2.0.CO;2

Lilly, D. K. (1978). A severe downslope windstorm and aircraft turbulence event induced by a mountain wave. *Journal of the Atmospheric Sciences*, *35*(1), 59-77. doi: 10.1175/1520-0469(1978)035⟨0059:ASDWAA⟩2.0.CO;2

McFarlane, N. A. (1987). The effect of orographically excited gravity wave drag on the general circulation of the lower stratosphere and troposphere. *Journal of Atmospheric Sciences*, *44*(14), 1775-1800. doi: 10.1175/1520-0469(1987)044⟨1775:TEOOEG⟩3E2.0.CO;2

Palmer, T. N., Shutts, G. J., & Swinbank, R. (1986). Alleviation of a systematic westerly bias in general circulation and numerical weather prediction models through an orographic gravity wave drag parametrization. *Quarterly Journal of the Royal Meteorological Society*, *112*(474), 1001-1039. doi: 10.1002/qj.49711247406

Perlwitz, J., & Graf, H. (2001). The variability of the horizontal circulation in the troposphere and stratosphere - a comparison. *Theoretical and Applied Climatology*, *69*(3-4), 149-161. doi: 10.1007/s007040170021

Preusse, P., Eckermann, S., & Ern, M. (2008). Transparency of the atmosphere to short horizontal wavelength gravity waves. *Journal of Geophysical Research: Atmospheres*, *113*(D24). doi: 10.1029/2007JD009682

Rapp, M., Drnbrack, A., & Preusse, P. (2018). Large midlatitude stratospheric

temperature variability caused by inertial instability: A potential source of bias for gravity wave climatologies. *Geophysical Research Letters*, *45*(19), 10,682-10,690. doi: 10.1029/2018GL079142

Reitebuch, O. (2012). The spaceborne wind lidar mission ADM-Aeolus. *Atmospheric Physics*, 815-827. doi: 10.1007/978-3-642-30183-4_49

Rennie, M., Tan, D., Andersson, E., Poli, P., Dabas, A., De Kloe, J., ... Stoffelen, A. (2020). Aeolus Level-2B Algorithm Theoretical Basis Document (Mathematical Description of the Aeolus L2B Processor). *ESA*, 124p.

Sato, K., Tateno, S., Watanabe, S., & Kawatani, Y. (2012). Gravity wave characteristics in the southern hemisphere revealed by a high-resolution middle-atmosphere general circulation model. *Journal of the Atmospheric Sciences*, *69*(4), 1378-1396. doi: 10.1175/JAS-D-11-0101.1

Siskind, D., Eckermann, S., Coy, L., McCormack, J., & Randall, C. (2007). On recent interannual variability of the Arctic winter mesosphere: Implications for tracer descent. *Geophysical Research Letters*, *34*(9). doi: 10.1029/2007GL029293

Stoffelen, A., Pailleux, J., Klln, E., Vaughan, J., Isaksen, L., Flamant, P., ... Meynart, R. (2005). The atmospheric dynamics mission for global wind field measurement. *Bulletin of the American Meteorological Society*, *86*(1). doi: 10.1175/BAMS-86-1-73

Strube, C., Ern, M., Preusse, P., & Riese, M. (2020). Removing spurious inertial instability signals from gravity wave temperature perturbations using spectral filtering methods. *Atmospheric Measurement Techniques*, *13*(9), 4927-4945. doi: /10.5194/amt-13-4927-2020

Sun, B., Reale, A., Seidel, D., & Hunt, D. (2010). Comparing radiosonde and COSMIC atmospheric profile data to quantify differences among radiosonde types and the effects of imperfect collocation on comparison statistics. *Journal of Geophysical Research: Atmospheres*, *115*(D23). doi: 10.1029/2010JD014457

Sun, C., Li, J., Jin, F., & Xie, F. (2014). Contrasting meridional structures of stratospheric and tropospheric planetary wave variability in the northern hemisphere. *Tellus A: Dynamic Meteorology and Oceanography*, *66*(1), 25303. doi: 10.3402/tellusa.v66.25303

Vincent, R., & Reid, I. (1983). HF Doppler measurements of mesospheric gravity wave momentum fluxes. *Journal of the Atmospheric Sciences*, *40*(5), 13211333. doi: 10.1175/1520-0469(1983)040⟨1321:HDMOMG⟩2.0.CO;2

Watanabe, S., Sato, K., Kawatani, Y., & Takahashi, M. (2015). Vertical resolution dependence of gravity wave momentum flux simulated by an atmospheric general circulation model. *Geoscientific Model Development*, *8*(6), 1637. doi: 10.5194/gmd-8-1637-2015

Wright, C., Hindley, N., Hoffmann, L., Alexander, M., & Mitchell, N. (2017). Exploring gravity wave characteristics in 3-D using a novel S-transform technique: AIRS/Aqua measurements over the Southern Andes and Drake Passage. *Atmospheric Chemistry and Physics*, *17*(13), 8553-8575. doi: 10.5194/acp-17-8553-2017

Wright, C., Hindley, N., & Mitchell, N. (2016). Combining AIRS and MLS observations for threedimensional gravity wave measurement. *Geophysical Research Letters*, *43*(2), 884-893. doi: 10.1002/2015GL067233

Wright, C., Hindley, N., Moss, A., & Mitchell, N. (2016). Multi-instrument gravity-wave measurements over Tierra del Fuego and the Drake Passage-Part 1: Potential energies and vertical wavelengths from AIRS, COSMIC, HIRDLS, MLS-Aura, SAAMER, SABER and radiosondes. *Atmospheric Measurement Techniques Discussions*, *8*(7). doi: 10.5194/amt-9-877-2016

Wright, C., Osprey, S., Barnett, J., Gray, L., & Gille, J. (2010). High Resolution Dynamics Limb Sounder measurements of gravity wave activity in the 2006 Arctic stratosphere. *Journal of Geophysical Research: Atmospheres*, *115*(D2).

586 doi: 10.1029/2009JD011858

Figure 1.

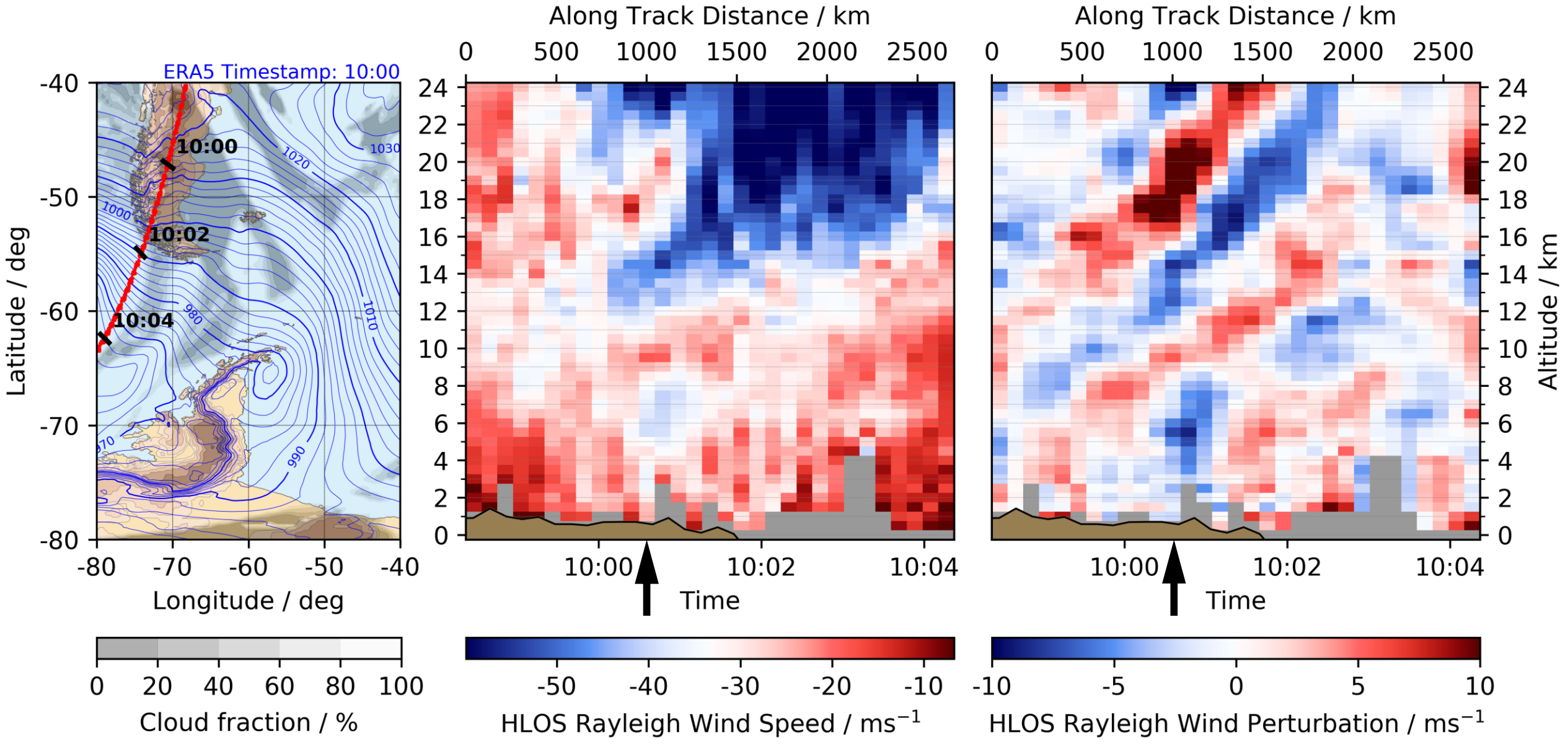
ERA5 Timestamp: 10:00
10:00
10:02
10:04
1030
1020
1000
980
1010
990
970
-40
-50
-60
-70
-80
Latitude / deg
Longitude / deg
Along Track Distance / km
0
500
1000
1500
2000
2500
24
22
20
18
16
14
12
10
8
6
4
2
0
Altitude / km
10:00
10:02
10:04
Time
0
20
40
60
80
100
Cloud fraction / %
-50
-40
-30
-20
-10
HLOS Rayleigh Wind Speed / ms^{-1}
-10
-5
0
5
10
HLOS Rayleigh Wind Perturbation / ms^{-1}

Figure 2.

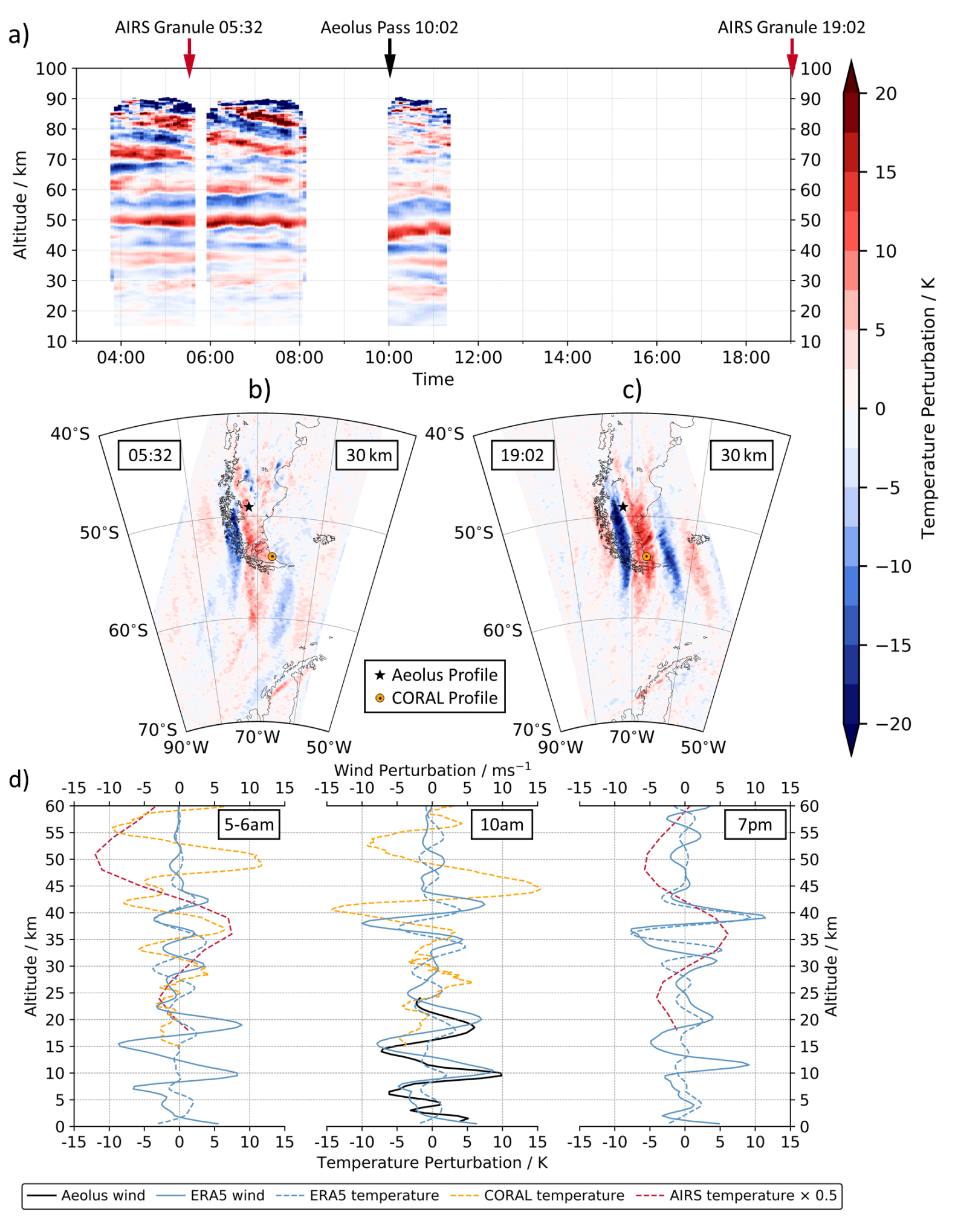
a)
AIRS Granule 05:32
Aeolus Pass 10:02
AIRS Granule 19:02
Altitude / km
Time
04:00
06:00
08:00
10:00
12:00
14:00
16:00
18:00
Temperature Perturbation / K
b)
c)
05:32
19:02
30 km
40°S
50°S
60°S
70°S
90°W
70°W
50°W
Aeolus Profile
CORAL Profile
d)
Wind Perturbation / ms^{-1}
5-6am
10am
7pm
Altitude / km
Temperature Perturbation / K
Aeolus wind
ERA5 wind
ERA5 temperature
CORAL temperature
AIRS temperature × 0.5

Figure 3.

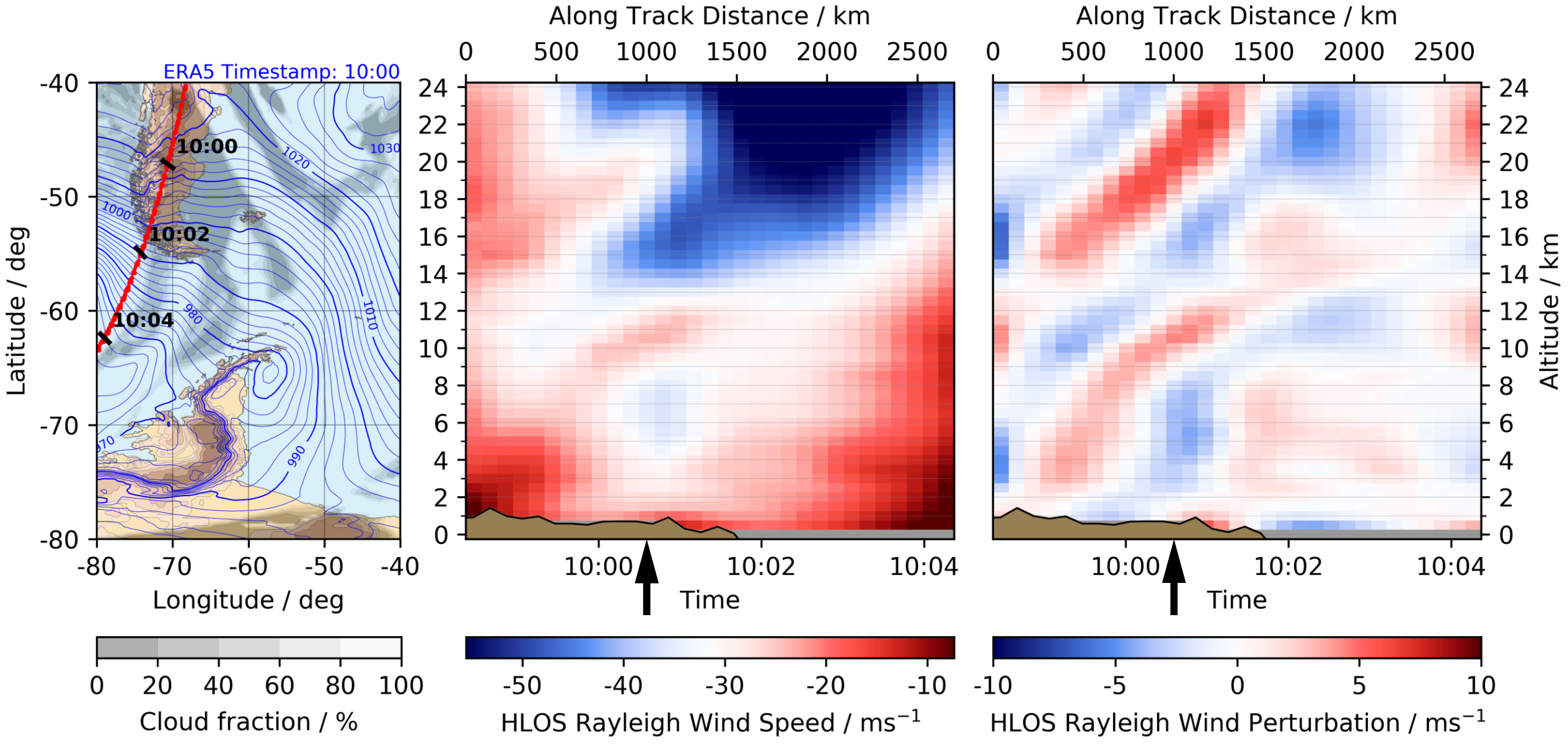
ERA5 Timestamp: 10:00
10:00
10:02
10:04
1030
1020
1000
980
1010
990
970
-40
-50
-60
-70
-80
Latitude / deg
-80
-70
-60
-50
-40
Longitude / deg
Along Track Distance / km
0
500
1000
1500
2000
2500
24
22
20
18
16
14
12
10
8
6
4
2
0
Altitude / km
10:00
10:02
10:04
Time
Along Track Distance / km
0
500
1000
1500
2000
2500
10:00
10:02
10:04
Time
0
20
40
60
80
100
Cloud fraction / %
-50
-40
-30
-20
-10
HLOS Rayleigh Wind Speed / ms^{-1}
-10
-5
0
5
10
HLOS Rayleigh Wind Perturbation / ms^{-1}